Available online at www.sciencedirect.com
ScienceDirect
Tetrahedron: Asymmetry
Tetrahedron: *Asymmetry* 17 (2006) 1937–1943

Enantioselective self-assembly, crystallographic structure and magnetic properties of the two enantiomers of the optically active canted antiferromagnet $[Ru(bpy)_3][Mn_2(ox)_3]$

Fabrice Pointillart, Cyrille Train,* Kamal Boubekeur, Michel Gruselle and Michel Verdaguer

Laboratoire de chimie Inorganique et Matériaux Moléculaire, CIM2 Unité CNRS 7071, Université Pierre et Marie Curie, 4 place Jussieu, case 42, 75252 Paris Cedex 05, France

Received 14 March 2006; accepted 29 June 2006
Available online 4 August 2006

Abstract—The two enantiomers of $[Ru(bpy)_3][Mn_2(ox)_3]$ (bpy = 2,2′-bipyridine, ox = oxalate), namely $[(\Delta)\text{-}Ru(bpy)_3][(\Delta)\text{-}Mn_2(ox)_3]$, (***Δ*-1**) and $[(\Lambda)\text{-}Ru(bpy)_3][(\Lambda)\text{-}Mn_2(ox)_3]$, (***Λ*-1**), were obtained as single crystals using $[(\Delta)\text{-}Ru(bpy)_3]^{2+}$ and $[(\Lambda)\text{-}Ru(bpy)_3]^{2+}$, respectively, as a chiral templating cation. Their structures were determined by single-crystal X-ray diffraction. The compounds crystallise in the enantiomeric chiral cubic space groups, $P4_332$ (***Δ*-1**) and $P4_132$ (***Λ*-1**), with $a = 15.492(2)$ and 15.507(2) Å, respectively ($Z = 4$). Both structures include a three-dimensional 10-gon 3-connected (10,3) anionic network wrapped around the $[Ru(bpy)_3]^{2+}$ cations. In both crystalline enantiomers, the resolved ruthenium template cation imposes both the topology and the absolute configuration of all the metal centres. The thermal variation of the magnetic susceptibility, measured on ***Δ*-1** and ***Λ*-1** crystals, reveals an antiferromagnetic coupling between the oxalate-bridged manganese ions in the paramagnetic region characterised by a negative Weiss constant $\Theta = -35$ K. Below $T_N = 13$ K, ***Δ*-1** and ***Λ*-1** exhibit a canted antiferromagnetic order.

1. Introduction

Over the past decade, oxalate-based materials have shown to be of particular importance in molecular magnetism, because of the versatility of the oxalate chemistry and the capability of the oxalate bridge to efficiently transmit the exchange interaction between two metal ions. This versatility has been exploited to introduce several physico-chemical properties in the same material leading to a wide variety of two- (2D) and three- (3D) dimensional multifunctional compounds.[1,2] Nevertheless, a few single-crystal structures have been described. This is even more obvious when one is interested by optically active materials obtained through enantioselective synthesis, since most of the X-ray structures described up to date have been determined on single crystals obtained by starting from racemic and achiral reagents for 2D[1] and 3D compounds. Chiral 3D structures of single crystals obtained from *racemic* reagents have actually been determined for compounds with general formula $[Fe^{II}(bpy)_3][Fe_2{}^{II}(ox)_3]$ (bpy = 2,2′-bipyridine, ox = oxalate),[3] $[Ni^{II}(bpy)_3][Mn_2{}^{II}(ox)_3]$, $[Fe^{II}(bpy)_3][Na^{I}Fe^{III}(ox)_3]$, $[Fe^{II}(bpy)_3][Li^{I}Cr^{III}(ox)_3]$,[4] $[M^{III}(bpy)_3][X][Na^{I}Cr^{III}(ox)_3]$ ($(M^{III}, X) = (Cr, ClO_4^-)$, (Co, PF_6^-)), $[Cr^{III}(bpy)_3][X][Mn_2{}^{II}(ox)_3]$ ($X = ClO_4^-, BF_4^-$) and $[Ni^{II}(phen)_3][Na^{I}Cr^{III}(dto)_3]$ (phen = (1,10)-phenantroline, dto = (1,2)-dithiooxalate),[5] $[Co^{III}(bpy)_3][ClO_4][Co_2{}^{II}(ox)_3]$,[6] $[M^{II}(bpy)_3][Li^{I}Cr^{III}(ox)_3]$ ($M = Ni, Ru$),[7] $[Ru^{II}(bpy)_3][ClO_4][Mn^{II}Cr^{III}(ox)_3]$,[8,9] $[Ru^{II}(bpy)_2(ppy)][Mn^{II}Cr^{III}(ox)_3]$ (ppy = 2-phenylpyridine-H^+)[8] and $[Ru^{II}(bpy)_3][Cu_2{}^{II}(ox)_3]$.[10] The only structures determined on single crystals obtained from *resolved* tris(diimiine)metal template cations associated with *racemic* tris(oxalato)chromate(III) and a third metal ion (Li^+, Mn^{2+}) are those of the (Δ)- and (Λ)-$[Ru^{II}(bpy)_3][Li^{I}Cr^{III}(ox)_3]$ paramagnets and of the (Δ)-$[Ru^{II}(bpy)_3][ClO_4][Mn^{II}Cr^{III}(ox)_3]$ ferromagnet ($T_C = 4.2$ K).[7,8] All these structures are composed of a 3D $[M_1M_2(ox)_3]^{n-}$ 10-gon 3-connected (10,3) anionic network wrapped around the $[M(bpy)_3]^{m+}$ cations. Since the octahedral environment of all the metal ions is made up of three bidentate ligands, the point group symmetry of all the metal centres is D_3. Due to the resulting helical chirality, every metal centre can exhibit either (Δ) or (Λ) configuration. The topology imposes the same configuration to all the metal ions and leads to homochiral compounds. Starting from racemic reagents, each crystal is chiral but (i) their configuration cannot be

* Corresponding author. E-mail: train@ccr.jussieu.fr

0957-4166/$ - see front matter © 2006 Elsevier Ltd. All rights reserved.
doi:10.1016/j.tetasy.2006.06.043

predicted and (ii) the crystals are often twinned. Moreover, a statistical assembly of crystals forms a conglomerate with no net optical activity.[11] The uncertainties brought about by an operating mode using racemic reagents make it unadaptable for studying the optical activity in these materials. Instead, the choice of the configuration of $[M^{II}(bpy)_3]^{2+}$ ($M^{II} = Ni, Ru$) allows us to control the configuration of the obtained material even on powders.[7,8,10] For powdered samples, light scattering prevents quantitative optical studies. Working on single crystals obtained by enantioselective crystal growth allows to overcome these problems.

Taking advantage of both the chiral templating activity of tris(diimine)ruthenium complexes and of their configurational stability,[7] we have grown single crystals of [(*Δ*)-Ru(bpy)$_3$][(*Δ*)-Mn$_2$(ox)$_3$], ***Δ*-1** and [(*Λ*)-Ru(bpy)$_3$]-[(*Λ*)-Mn$_2$(ox)$_3$], ***Λ*-1** from $[(\Delta)\text{-Ru(bpy)}_3]^{2+}$ and $[(\Lambda)\text{-Ru(bpy)}_3]^{2+}$, respectively, as unique building blocks. The structures of both enantiomers are described as well as their magnetic properties.

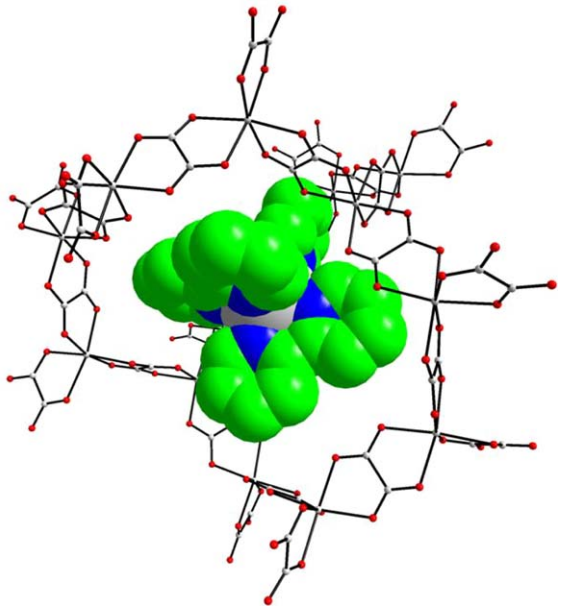

Figure 1. A decagon of the anionic network is wrapped around the template cation (shown for ***Δ*-1**).

2. Results and discussion

2.1. Synthesis and single-crystal growth

Before undertaking single-crystal growth of ***Δ*-1** and ***Λ*-1**, several steps were required. The first one was to check the ability of $[M^{II}(bpy)_3]^{2+}$ to template the formation of the 3D oxalate-bridged $[Mn_2{}^{II}(ox)_3]^{2-}$ anionic networks starting from the 'naked' Mn^{2+} ions.[4,7] The self-assembly process begins with an isotropic interaction between a negatively charged oxalate and a cationic tris(diimine)metal complex. Strong oxalato···phenyl interactions similar to those reported by Dance et al. on the 3D $(Ph_3MeP)_2$-$[Na^{I}Cr^{III}(ox)_3]$ compound[12] orientate the oxalate with respect to the diimine ligand. Step by step wrapping of manganese and oxalate ions around the D_3 template cation (Fig. 1) then led to the formation of the (10,3) anionic network. In order to ensure the closure of the 10-gons, the tris(diimine) cation and the anionic network must be compatible in size. In the present case, we found that $[Ru^{II}(bpy)_3]^{2+}$ works much better than $[Ru^{II}(phen)_3]^{2+}$ (phen = 1,10-phenantroline) in helping with the formation of the $[Mn_2{}^{II}(ox)_3]^{2-}$ anionic network while Decurtins et al.[5] showed that $[Ni^{II}(phen)_3]^{2+}$ templates the formation of the $[Na^{I}Co^{III}(dto)_3]^{2-}$ anionic network because of the enhanced size of the (1,2)-dithiooxalate ligand compared to the oxalate. The templating activity of the D_3 $[M^{II}(bpy)_3]^{2+}$ cations is efficient not only because their symmetry is well adapted to the formation of (10,3) anionic network, but also due to their charge and size.

The next step was to measure the natural circular dichroism (NCD) to show that it was possible to obtain enriched compounds starting from the resolved template cation.[7] This first set of experiments allowed us to assess the chiral templating activity of $[Ru^{II}(bpy)_3]^{2+}$ towards the formation of optically active 3D oxalate-bridged $[Mn_2{}^{II}(ox)_3]^{2-}$ anionic networks.[7]

Exploiting the remarkable configurational stability of tris(bischelated)ruthenium(II) complexes, which directly derives from the kinetic inertness of these d^6 low spin species, the last step was to grow single crystals of $[(\Lambda)\text{-}Ru^{II}(bpy)_3][(\Lambda)\text{-}Mn_2{}^{II}(ox)_3]$ and $[(\Delta)\text{-}Ru^{II}(bpy)_3]$-$[(\Delta)\text{-}Mn_2{}^{II}(ox)_3]$ starting from (Λ)-$[Ru^{II}(bpy)_3]^{2+}$ and (Δ)-$[Ru^{II}(bpy)_3]^{2+}$, respectively, mixed with free oxalate and aqua complex of manganese(II). Slow diffusion of the reactants allowed us to perform the crystallisation by enantio-

Table 1. Selected bond distances (Å) and angles (°) for ***Δ*-1** in $P4_332$

Ru(1)–N(1)	2.057(4)	Mn(1)–O(1)	2.167(5)
		Mn(1)–O(2)	2.133(5)
N(1)#1–Ru(1)–N(1)#4	91.3(3)	O(2)#1–Mn(1)–O(2)	91.03(18)
N(1)#1–Ru(1)–N(1)#3	95.1(2)	O(2)–Mn(1)–O(1)#1	93.8(2)
		O(1)#1–Mn(1)–O(1)#3	97.82(16)
N(1)#1–Ru(1)–N(1)#2	79.1(3)	O(2)#1–Mn(1)–O(1)#1	78.08(17)
N(1)#2–Ru(1)–N(1)#3	171.8(3)	O(2)#3–Mn(1)–O(1)#1	168.17(19)

Symmetry transformations used to generate equivalent atoms

#1 $z+1/2, -x+1/2, -y$	#2 $-z+1/4, -y+1/4, -x+1/4$
#3 $-y+1/2, -z, x-1/2$	#4 $-x+3/4, z+1/4, y-1/4$
#5 $y+1/4, x-1/4, -z-1/4$	#6 $-y+1/4, -x+1/4, -z-3/4$

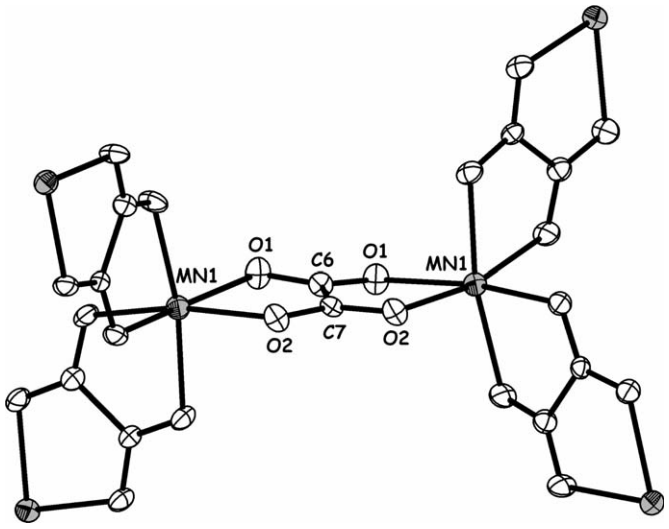

Figure 2. Ortep view of a representative section of the 3D $[Mn_2^{II}(ox)_3]^{2-}$ anionic network of the crystal structure of ***Λ*-1**. Displacement ellipsoids are shown at the 50% probability level.

selective self-assembly of the anionic network around the cationic unit.

2.2. Structure

Selected bond distances and angles for ***Λ*-1** and ***Δ*-1** are listed in Table 1. The crystal structure of ***Λ*-1** consists of tris(oxalato)manganate(II) moieties (Fig. 2) arranged in order to form a three-dimensional 10-gon 3-connected nets (10,3) oxalate-based anionic network (Fig. 3a) composed of interconnected helices (Fig. 4) going in the three directions of space. The $[Ru^{II}(bpy)_3]^{2+}$ cations are situated in the vacancies of the anionic network (Fig. 1). The space group is $P4_132$, a chiral cubic space group where all the tris(bischelated) manganese ions adopt the (*Λ*) configuration. In the (*Λ*)-$[Ru^{II}(bpy)_3]^{2+}$ cation, the six nitrogen atoms are at the same distance from the Ru(II) cation, 2.059 Å. In the anionic network $[Mn_2^{II}(ox)_3]^{2-}$, the manganese atoms are located on the 3-fold axis. They are surrounded by 3 equiv oxygen atoms O(1) located at 2.133 Å and three other equivalent oxygen atoms O(2) located at 2.168 Å with an O(2)–Mn(1)–O(1) angle of

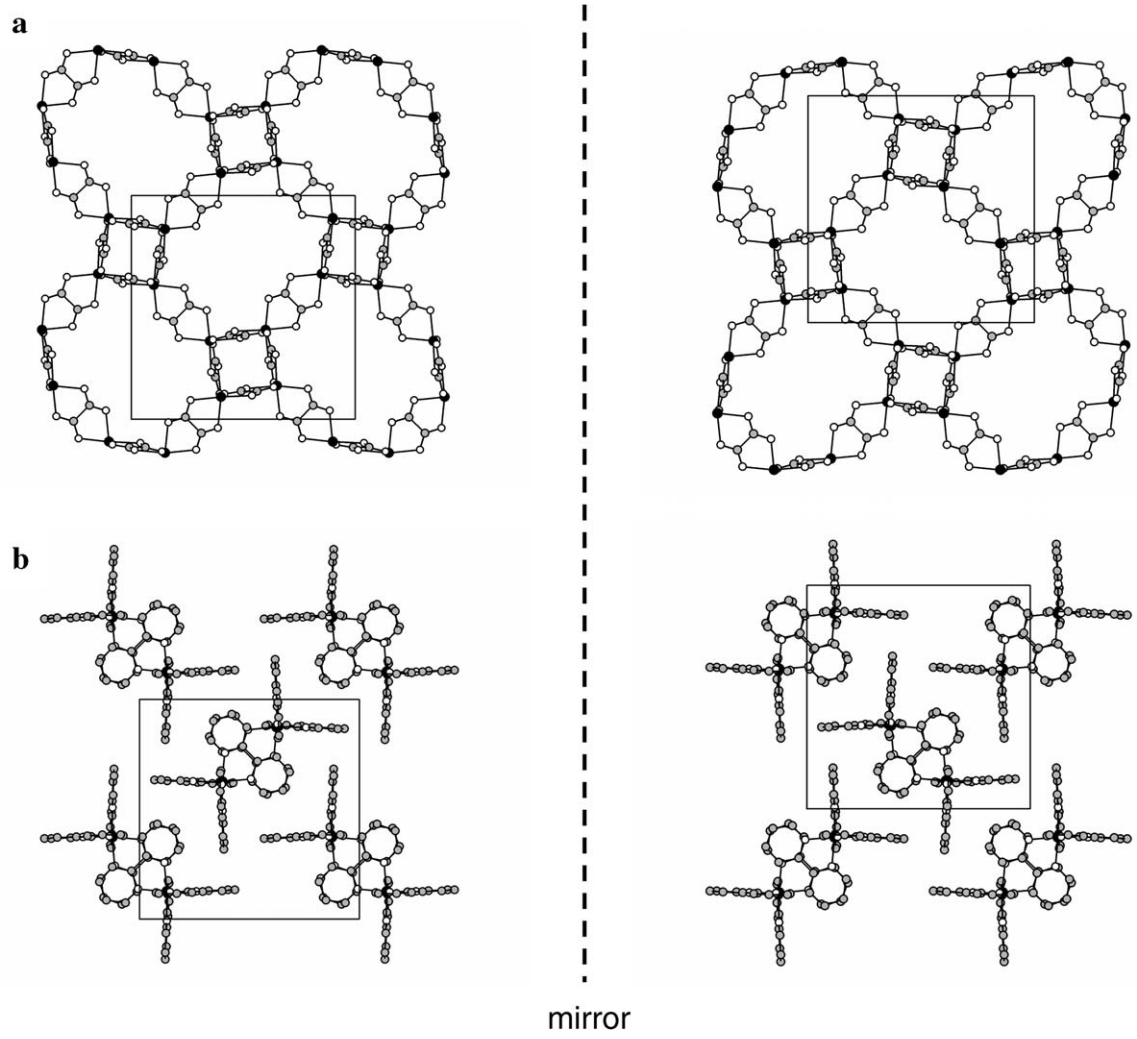

Figure 3. Projection of the structures of the two enantiomers ***Δ*-1** (left) and ***Λ*-1** (right) along [1 0 0] showing the mirror images of the anionic networks (a) and of the template cations (b).

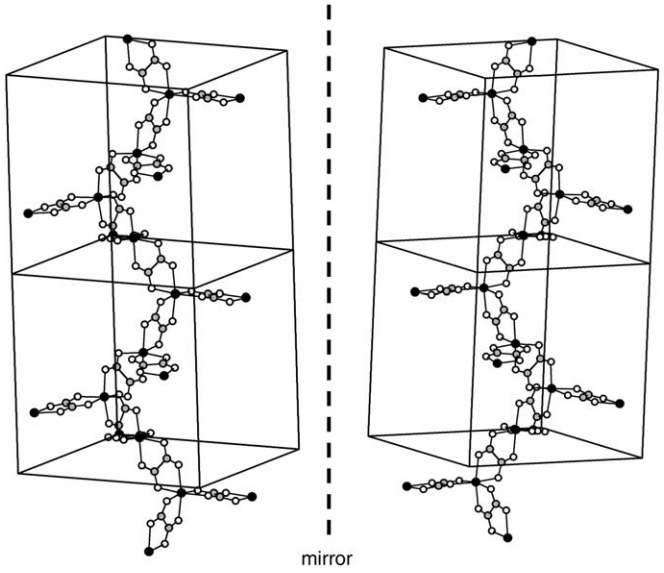

Figure 4. Left-(M) in *Δ*-**1** (left) and right-(P) in *Λ*-**1** (right) handed helices going along *z*. Oxalate ligands lying along the *x* and *y* axes allow the growth of helices in these directions as shown in Figure 3a.

78.1° leading to a slightly trigonally compressed octahedral environment. The oxalate bridge presents two different C–O distances, 1.236 and 1.256 Å, in a *cis* conformation (Fig. 2). The crystal structure of *Δ*-**1** is within the experimental precision, the mirror image of *Λ*-**1** (Figs. 3 and 4).

The crystal structures of *Δ*-**1** and *Λ*-**1** were compared with that of $[Ni^{II}(bpy)_3][Mn_2{}^{II}(ox)_3]$.[4] The Ru–N distance (2.057 Å) in **1** is shorter than the Ni–N distance (2.088 Å) in the latter compound. This is related to the electronic structure of the two ions, $t_{2g}{}^6e_g^0$ (octahedral d^6 low spin complex) for Ru(II) and $t_{2g}{}^6e_g^{*2}$ (octahedral d^8 complex) for Ni(II). In the latter case, the antibonding e_g^* orbitals are partially filled, while they are empty in the former case, leading to a slight increase of the Ni(II)–N distances compared to Ru(II)–N ones. This trend compares well with the one observed when going from $[Ru^{II}(bpy)_3][PF_6]_2$ to $[Ni^{II}(bpy)_3][PF_6]_2$, where the mean M–N distance at 200 K in the γ phase goes from 2.063 Å for Ru to 2.083 Å for Ni.[13] A noticeable change when going from γ-$[Ru^{II}(bpy)_3][PF_6]_2$ to *Δ*-**1** and *Λ*-**1** was the strong modification of the torsion angle between the two pyridine cycles of the bipyridine ligand. In the former salt, it varies from 6.7° up to 12.7° while it is less than 1° in *Δ*-**1** and *Λ*-**1**. The same observation holds when comparing the geometry of $[Ni^{II}(bpy)_3]^{2+}$ in γ-$[Ni^{II}(bpy)_3][PF_6]_2$[13] and in $[Ni^{II}(bpy)_3][Mn_2{}^{II}(ox)_3]$.[4] We assign these torsion angle modifications to the influence of the anionic network on the template cation through the oxalato···phenyl interactions.[12] The changes in the geometry of the template cation reveal that the first coordination sphere, as well as the bischelating ligand of the tris(bischelated)cations, are rigid enough to impose the topology of the anionic network, but flexible enough to suit the packing requirements of the final compound.

In the anionic network, the Mn(II) environment was trigonally distorted both in **1** and in $[Ni^{II}(bpy)_3][Mn_2{}^{II}(ox)_3]$. Due to both σ- and π-donations from the ligand, the shorter Mn–O distance (2.135 Å in **1**, 2.154 Å in $[Ni(bpy)_3][Mn_2(ox)_3]$) corresponds to the longer O–C (1.236 Å in **1**, 1.241 Å in $[Ni^{II}(bpy)_3][Mn_2{}^{II}(ox)_3]$). The average Mn–O distance was 2.151 Å in **1** and 2.160 Å in $[Ni^{II}(bpy)_3][Mn_2{}^{II}(ox)_3]$. The distortion was larger in **1** than in $[Ni^{II}(bpy)_3][Mn_2{}^{II}(ox)_3]$. These data demonstrate that there exists a close relationship between the structure of the template cation, the overall structure and the structure of the anionic network: smaller M–N distances in the template cation lead to smaller cell parameters and to a reduced size of the anionic network. The size enhancement of the template cation when going from Ru(II) to Ni(II) is accommodated by both an increase of the Mn–O mean distance and by a modification of the trigonal distortion of the Mn environment. The balance between these two parameters is the result of the interplay between the internal constraints existing in the coordination-bonded anionic network and the adaptation of this network to the template cation through supramolecular interactions.

2.3. Magnetic properties

The thermal variation of χ_M for *Δ*-**1** (Fig. 5a) and *Λ*-**1** shows a monotonic increase when the temperature is

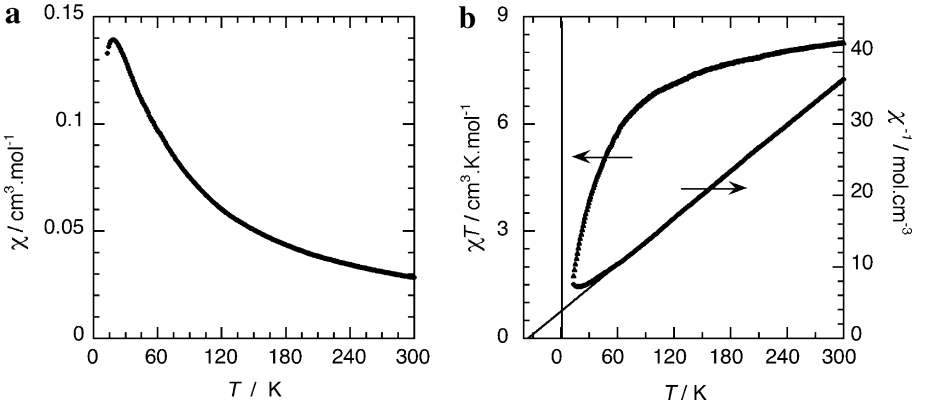

Figure 5. Thermal variations of χ_M (a), $\chi_M T$ (left axis) and χ_M^{-1} (right axis) (b) of *Δ*-**1** measured using a 0.1 T magnetic field. In the latter case, the Curie-Weiss fit appears as a straight line.

decreased down to 18 K, where it exhibits a rounded maximum. The magnetic properties of both enantiomers are identical within experimental errors. The results obtained for *Δ*-**1** are shown in Figures 5 and 6. The $\chi_M T$ product decreases continuously from 8.31 cm^{-3} K mol^{-1} at 300 K when the temperature is lowered (Fig. 5b). The χ_M^{-1} versus T curve (Fig. 5b) is linear in the 100–300 K temperature range. It can be fitted by a Curie–Weiss law $\chi_M^{-1} = (T - \Theta)/C$ leading to a negative Weiss constant Θ of −35 K. The Zero Field Cooled (ZFC), Field Cooled (FC) and remnant magnetisation versus temperature curves are shown in Figure 6. The remnant magnetisation of *Δ*-**1** and *Λ*-**1** disappears when the temperature becomes higher than $T_N = 13$ K. This temperature corresponds to the intersection of the ZFC and FC curves. The first magnetisation curve at 2 K is linear up to 5 T where it reaches 1.6 μ_B, far from the saturation value of the material (10 μ_B).

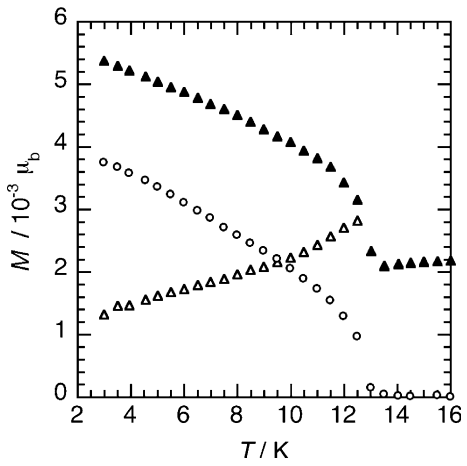

Figure 6. Zero Field Cooled (open triangles), Field Cooled (triangles) and Remnant magnetisation (open circles) of *Δ*-**1** measured using a 0.01 T magnetic field.

The general shape of the $\chi_M T$ versus T curve, the value of the $\chi_M T$ product, which is lower for all T than 8.75 cm^{-3} K mol^{-1}, the value expected for two independent manganese ions with $S = 5/2$ and $g = 2$, are characteristic of a noticeable antiferromagnetic coupling between the two manganese ions in the 3D anionic network. The antiferromagnetic exchange interaction between the manganese ions through the oxalate bridge is supported by the negative value of the Weiss constant ($\Theta = -35$ K). These results compare well with those obtained for $[Fe^{II}(bpy)_3][Mn_2{}^{II}(ox)_3]$.[4,14] The overall behaviour of **1** and $[Fe^{II}(bpy)_3][Mn_2{}^{II}(ox)_3]$ is the same because it is dominated by the antiferromagnetic (AF) coupling between the manganese ions in the 3D anionic network. The increase of the absolute values of Θ and T_N in **1** compared to $[Fe^{II}(bpy)_3][Mn_2{}^{II}(ox)_3]$ is attributed to (i) the absence of paramagnetic impurities thanks to the use of single crystals to perform the measurements; (ii) slight changes in the structure of the anionic network due to the use of a different template cation.[8] The ZFC/FC/remnant sequence

Table 2. Crystal data and structure refinement for *Δ*-**1** and *Λ*-**1**

Crystal data		
Compound	*Δ*-**1**	*Λ*-**1**
Empirical formula	$C_{36}H_{24.50}Mn_2N_6O_{12.25}Ru$	
Formula weight	948.07	
Crystal system, space group	Cubic, $P4_332$ (No. 212)	Cubic, $P4_132$ (No. 213)
Unit cell dimensions	$a = 15.492(2)$ Å	$a = 15.507(2)$ Å
Volume	3718.1(8) $Å^3$	3728.9(8) $Å^3$
Z, Calculated density	4, 1.694 g cm^{-3}	4, 1.689 g cm^{-3}
Absorption coefficient (Mo Kα)	1.143 mm^{-1}	1.140 mm^{-1}
$F(000)$	1898	
Data collection		
Temperature	253(2) K	
Wavelength	0.71073 Å	
Crystal size	0.20 × 0.18 × 0.16 mm	0.18 × 0.16 × 0.14 mm
Theta range	3.72–30.00°	2.94–29.96°
Limiting indices	$-21 \leqslant h, k, l \leqslant 21$	$-21 \leqslant h, k, l \leqslant 21$
Reflections collected/unique	72769/1823 [$R_{int} = 0.0429$]	62107/1822 [$R_{int} = 0.0508$]
Completeness to theta = 30.00	99.6%	99.5%
Absorption correction	Semi-empirical from equivalents	
Max. and min. transmission	0.7902 and 0.7525	0.9087 and 0.8655
Refinement		
Refinement method	Full-matrix least-squares on F^2	
Data/restraints/parameters	1824/3/86	1822/3/86
Observed data [$I > 2.0$sigma(I)]	1447	1367
Goodness-of-fit on F^2	1.056	1.051
Final R indices [$I > 2$sigma(I)]	$R1 = 0.0639$, $wR2 = 0.1573$	$R1 = 0.0676$, $wR2 = 0.1636$
R indices (all data)	$R1 = 0.0895$, $wR2 = 0.1733$	$R1 = 0.1022$, $wR2 = 0.1933$
Absolute structure parameter	0.02(4)	0.04(5)
Max. and Av. shift/error	0.00/0.00	0.00/0.00
Largest diff. peak and hole	2.300 and −2.772 e $Å^{-3}$	2.051 and −2.663 e $Å^{-3}$

demonstrates the existence of a long range magnetic order below $T_N = 13$ K. The absolute value of the magnetisation observed in the Field Cooled curve is three orders of magnitude lower than those observed in the parent ferromagnetic 3D compounds[8] in accordance with the expected AF ordering.[4] The appearance of a weak remnant magnetisation below T_N can be ascribed to a weak canting of the magnetic moments in the AF phase. Such a phenomenon has already been observed in $[Co^{III}(bpy)_3][ClO_4]$-$[Co_2^{II}(ox)_3]$, a parent 3D oxalate-based compound.[6] In the $[Co_2^{II}(ox)_3]^{2-}$ anionic network, an explanation of the canting based on the single-ion anisotropy was proposed. In $[Mn_2^{II}(ox)_3]^{2-}$, single-ion anisotropy can be ruled out. More suitably, canting can be explained by the occurrence of an antisymmetric Dzyaloshinsky–Moriya magnetic exchange. This mechanism is indeed made possible by the non-centrosymmetric space group observed in these compounds.

3. Conclusion

The self-assembly of the $[Mn_2^{II}(ox)_3]^{2-}$ 10-gon 3-connected anionic network, as well as the transfer at the crystal level of the chirality of the configurationally stable tris(bipyridine)ruthenium(II) cation, has been described. This first enantioselective single-crystal growth of 3D oxalate-based networks, in the case when tris(oxalato)metallate D_3 symmetry preformed building blocks are not available, can be considered as a general strategy to insert almost any metal ion in crystalline resolved 3D oxalate-based networks. Since single crystals are ideal objects for precise magnetic and optical measurements, this strategy is valuable to perform systematic studies on these multifunctional compounds.

4. Experimental

4.1. Materials

We have followed experimental procedures described in the literature to prepare $[Ru(bpy)_3]X_2$ $(X = Cl, I)$[15] and the enantiomerically enriched (Δ)- and (Λ)-isomers of $[Ru(bpy)_3]I_2{\cdot}3H_2O$.[16] The other reagents are commercially available and were used as purchased.

4.2. Single crystal growth

A typical crystallisation experiment consists of the formation of a silica gel by mixing $Si(OCH_3)_4$ (2 cm^3), CH_3OH (2 cm^3) and a 2 cm^3 aqueous solution containing 7.6 mg of oxalic acid. The resulting colourless solution is then placed in a test tube. After a few days, a gel is formed and an aqueous solution (6 cm^3) containing 37.8 mg of (Λ)- or (Δ)-$[Ru(bpy)_3]I_2{\cdot}6H_2O$ (0.049 mmol) and 15.6 mg of $Mn(NO_3)_2{\cdot}6H_2O$ (0.055 mmol) is added. After 2 weeks, tetrahedral-shaped dark red crystals form.

4.3. Physical techniques

The magnetisation of slightly crushed single crystals were measured between 2 and 300 K on a Quantum Design MPMS5 squid magnetometer. The susceptibility was measured in a 0.1 T external field and corrected for temperature-independent effects. The hysteresis loops was measured at 2 K. The zero field cooled and field cooled measurements were performed in a 0.01 T external field. The thermal variation of remnant magnetisation was measured after applying the same field. Prior to these measurements, the superconducting coil was treated in order to eliminate any remnant external field.

4.4. Single crystal structure determination

With the studied compounds being slightly moisture sensitive, single crystals were swiftly transferred with a small amount of solution to paratone-N oil, selected, mounted onto a glass fibre and cryocooled in a chilled nitrogen gas stream. Diffraction data were then collected, using a combination of ω and 2θ scans, on a Nonius Kappa-CCD diffractometer at 253 K for Δ-**1** and Λ-**1** (Table 2). Unit cell parameters determination, data collection strategy and integration were carried out with the Nonius EVAL-14 suite of programs.[17] The data were corrected from absorption by a multiscan method.[18] The structures were solved by direct methods with SHELXS-86,[19] refined by full least-squares on F^2 and completed with SHELXL-97.[20] Graphics were carried out with DIAMOND.[21] All non-H atoms were refined with anisotropic displacement parameters. The H atoms despite being visible on the ΔF-map, were simply introduced at calculated positions (riding model) except those of the water molecules (located on the threefold axis) for which the identified positions were first used then allowed to ride.

The absolute configurations of Δ-**1** and Λ-**1** were clearly established, with Flack's x-parameter of 0.02(4) and 0.04(5), respectively.[22] Thus the space group choice was $P4_332$ and $P4_132$, respectively. No twinning of merohedry was observed for the measured crystals. Values of 6.4% and 6.8%, respectively, were obtained for the R-factor and 15.7% and 16.4%, respectively, for the weighted R-factor.

Acknowledgements

The authors thank CNRS (France), Université Pierre et Marie Curie (France), DFG Schwerpunktprogramm 'Molekularer Magnetismus' (SPP 1137) and the European Network of Excellence Magmanet for financial support. The authors thank Christophe Cartier dit Moulin for fruitful scientific discussions.

References

1. Pilkington, M.; Decurtins, S. In *Magnetism: Molecules to Materials*; Miller, J. S., Drillon, M., Eds.; Wiley-VCH: Weinheim, Germany, 2001; Vol. II, pp 338–356.
2. Clement, R.; Decurtins, S.; Gruselle, M.; Train, C. In *Molecular Magnets: Recent Highlights*; Linert, W., Verdaguer, M., Eds.; Springer: Wien, New York, 2003; pp 1–20.
3. Decurtins, S.; Schmalle, H. W.; Schneuwly, P.; Oswald, H. R. *Inorg. Chem.* **1993**, *32*, 1888–1892.

4. Decurtins, S.; Schmalle, H. W.; Schneuwly, P.; Ensling, J.; Guetlich, P. *J. Am. Chem. Soc.* **1994**, *116*, 9521–9528.
5. Decurtins, S.; Schmalle, H. W.; Pellaux, R.; Schneuwly, P.; Hauser, A. *Inorg. Chem.* **1996**, *35*, 1451–1460.
6. Hernandez-Molina, M.; Lloret, F.; Ruiz-Perez, C.; Julve, M. *Inorg. Chem.* **1998**, *37*, 4131–4135.
7. Andres, R.; Gruselle, M.; Malezieux, B.; Verdaguer, M.; Vaissermann, J. *Inorg. Chem.* **1999**, *38*, 4637–4646.
8. Andres, R.; Brissard, M.; Gruselle, M.; Train, C.; Vaissermann, J.; Malezieux, B.; Jamet, J.-P.; Verdaguer, M. *Inorg. Chem.* **2001**, *40*, 4633–4640.
9. Coronado, E.; Galan-Mascaros, J. R.; Gomez-Garcia, C. J.; Martinez-Agudo, J. M. *Inorg. Chem.* **2001**, *40*, 113–120.
10. Pointillart, F.; Train, C.; Gruselle, M.; Villain, F.; Schmalle, H. W.; Talbot, D.; Gredin, P.; Decurtins, S.; Verdaguer, M. *Chem. Mater.* **2004**, *16*, 832–841.
11. Jacques, J.; Collet, A.; Wilen, S. H. *Enantiomers, Racemates and Resolutions*; Wiley: New York, 1981.
12. Russell, V. M.; Craig, D. C.; Scudder, M. L.; Dance, I. C. *Cryst. Eng. Comm.* **2000**, 3–10.
13. Breu, J.; Domel, H.; Stoll, A. *Eur. J. Inorg. Chem.* **2000**, 2401–2408.
14. Decurtins, S.; Schmalle, H. W.; Pellaux, R.; Huber, R.; Fischer, P.; Ouladdiaf, B. *Adv. Mater.* **1996**, *8*, 647–651.
15. Broomhead, J. A.; Young, C. G. *Inorg. Synth.* **1982**, *21*, 127–128.
16. Dwyer, F. P.; Gyarfas, E. C. *J. Proc. R. Soc. NSW* **1949**, *83*, 174.
17. Duisenberg, A. J. M.; Kroon-Batenburg, L. M. J.; Schreurs, A. M. M. *J. Appl. Crystallogr.* **2003**, *36*, 220–229.
18. Blessing, R. H. *Acta Cryst.* **1995**, *A51*, 33–38.
19. Sheldrick, G. M. SHELXS86, *Computer Program for Structure Solution*; University of Göttingen: Germany, 1986.
20. Sheldrick, G. M. SHELXL97, *Computer Program for Structure Refinement*; University of Göttingen: Germany, 1997.
21. Brandenburg, K.; Berndt, M. *Diamond*; Crystal Impact GbR: Bonn, Germany, 1999.
22. Flack, H. D.; Bernardinelli, G. *Acta Cryst.* **1999**, *A55*, 908–915; Flack, H. D.; Bernardinelli, G. *J. Appl. Crystallogr.* **2000**, *33*, 1143–1148.